

TOOLS AND TECHNIQUES

Non-invasive single-cell biomechanical analysis using live-imaging datasets

Yanthe E. Pearson^{1,*}, Amanda W. Lund², Alex W. H. Lin³, Chee P. Ng^{4,5}, Aysha Alsuwaidi⁶, Sara Azzeh⁶, Deborah L. Gater¹ and Jeremy C. M. Teo^{6,*‡}

ABSTRACT

The physiological state of a cell is governed by a multitude of processes and can be described by a combination of mechanical, spatial and temporal properties. Quantifying cell dynamics at multiple scales is essential for comprehensive studies of cellular function, and remains a challenge for traditional end-point assays. We introduce an efficient, non-invasive computational tool that takes time-lapse images as input to automatically detect, segment and analyze unlabeled live cells; the program then outputs kinematic cellular shape and migration parameters, while simultaneously measuring cellular stiffness and viscosity. We demonstrate the capabilities of the program by testing it on human mesenchymal stem cells (huMSCs) induced to differentiate towards the osteoblastic (huOB) lineage, and T-lymphocyte cells (T cells) of naïve and stimulated phenotypes. The program detected relative cellular stiffness differences in huMSCs and huOBs that were comparable to those obtained with studies that utilize atomic force microscopy; it further distinguished naïve from stimulated T cells, based on characteristics necessary to invoke an immune response. In summary, we introduce an integrated tool to decipher spatiotemporal and intracellular dynamics of cells, providing a new and alternative approach for cell characterization.

KEY WORDS: Cell biomechanics, Live imaging, Mechanobiology, T-lymphocyte cells, Mesenchymal stem cells, Cell migration

INTRODUCTION

Cell stiffness is a widely used measure for cellular biomechanics, and has been used to differentiate between healthy and diseased cells (Cross et al., 2007; Lim et al., 2010), cells in their diverse phenotypic states (Ekpenyong et al., 2012; Swaminathan et al., 2011) and cells acting in response to varying external biophysical stimuli (Kumar, 2014; Provenzano and Keely, 2011). An example is the increased cellular stiffness of fibroblasts when adhered to substrates of increasing firmness (Gupta et al., 2015; Solon et al., 2007). By and large, the stiffness of a cell is dictated by its cytoskeleton, a highly dynamic network of interconnected proteins that supports the cell,

giving it shape, and is responsible for cellular processes such as migration, receptor internalization, endocytosis, exocytosis, and interactions with the surrounding substrate and neighboring cells (Baker et al., 2010; Kim and Coulombe, 2010). The cytoskeleton is also the amalgamating center for inbound intracellular signals from biophysical cues and outbound communication transduction pathways from the nucleus, acting as a vital information highway necessary for cell maintenance, homeostatic regulation and locomotion (Bezanilla et al., 2015; Mullins, 2010). As such, the cytoskeleton is a clear link between cellular biomechanics and biological function; therefore, quantifying single-cell biomechanical properties as a physiological metric has become vital in cell biology research.

The technical limitations of many current cellular biomechanical measurement protocols hinder their usefulness in studies that investigate cell physiology under *in vivo* or truly biomimetic conditions. Biomechanical measurements using whole-cell deformation approaches, such as micropipette aspiration (Key and Robinson, 2013), optical tweezers (Ekpenyong et al., 2012), substrate stretching (Bartalena et al., 2011) or the microplate stretcher (Hoffman and Crocker, 2009), yield global easy-to-interpret single-cell measurements of biomechanical stiffness; however, such methods require detaching otherwise adherent cells or placing cells on a less biologically relevant substrate. Furthermore, techniques such as atomic force microscopy (AFM) (Haase and Pelling, 2015) and magnetic twisting cytometry (Massiera et al., 2007) utilize nano-sized physical probes to acquire biomechanical readings at subcellular regions of interest, acquiring information of superior spatial resolution; at this scale, however, intracellular non-uniformity causes considerable variability in measured biomechanical responses, exacerbating the already present heterogeneity in many cell populations. Most importantly, these current techniques are unable to measure or acquire dynamic mechanical properties adequately; for example, data acquisition using AFM takes ~15 min, but cells frequently change shape at the millisecond to minute range, and is also not compatible with high-throughput studies. Optical imaging can capture images at time scales that are more physiologically relevant than AFM (Haase and Pelling, 2015; Suresh, 2007). There is an increasing interest in recreating the cellular microenvironment through the introduction of appropriate and controlled biophysical cues to the cells; for example, by designing custom micro-fluidic-based cell culture chambers to mimic *in vivo* environments of fluid flow. Equally, in a move away from traditional, yet limiting, two-dimensional culture, some devices incorporate three-dimensional matrices to house cells (Haessler et al., 2011; Pisano et al., 2015) several of which allow live imaging during the exposure of cells to bound and soluble cytokine sources (Polacheck et al., 2011), and mechanical forces such as fluid shear stresses of different magnitudes (Haessler et al., 2012). In comparison, intravital

¹Department of Applied Mathematics and Sciences, Khalifa University, P.O. Box 127788, Abu Dhabi, UAE. ²Department of Cell, Developmental and Cancer Biology, Oregon Health and Science University, Portland, OR 97239, USA.

³Endothelix, Inc., 2500 West Loop, South Houston, TX 77027, USA. ⁴Singapore-MIT Alliance for Research and Technology, 1 CREATE Way, Singapore 138602.

⁵Mimetas BV, JH Oortweg 19, Leiden 2333 CH, The Netherlands. ⁶Department of Biomedical Engineering, Khalifa University, P.O. Box 127788, Abu Dhabi, UAE.

*These authors contributed equally to this work

‡Author for correspondence (jeremy.teo@kustar.ac.ae)

Y.E.P., 0000-0002-5662-1389; A.W.H.L., 0000-0002-2053-5139; C.P.N., 0000-0002-4508-2770; S.A., 0000-0001-9586-1214; D.L.G., 0000-0001-5353-8179; J.C.M.T., 0000-0001-6869-3833

imaging uses an actual *in vivo* system as a cell culture chamber whereby cells of interest are marked fluorescently and imaging is performed *in situ* (Kilariski et al., 2013). The aforementioned biomechanical evaluation techniques are challenging to implement *in vivo* or in complex biomimetic *in vitro* environments with minimal perturbations; inherent background noise arising from motion of the matrices or fluid forces present in more complex systems could also mask cellular information.

Current *in situ* biomechanical measurement strategies, namely traction force microscopy (TFM) and particle-tracking microrheology (PTMR), require the introduction of foreign fluorescent particles in the surrounding matrix (Hall et al., 2013) or within the cells themselves (Wirtz, 2009). For the case of TFM, matrix-embedded fluorescent particles and adjacent cells are tracked by fluorescent image microscopy: as cell locomotion deforms the matrices, pericellular particles are displaced accordingly. Particle displacement fields are measured using digital image correlation algorithms followed by surface traction estimates. Although this is not a direct measurement of cell stiffness, the resultant cellular interaction with the immediate surrounding substrate is assumed to be a surrogate measure of the biomechanical state of the cell. More advanced approaches make use of computationally expensive finite element methods to bridge the gap between particle displacement and intracellular mechanical properties, as an approximation of cell stiffness (Zielinski et al., 2013). For the case of PTMR, as there is intimate contact between the particles and intracellular structures, movement of the particles within live cells is quantified through the mean squared displacement (MSD) and interpreted as a proportional quantifier of the mechanical state of the cells, otherwise known as the complex viscoelastic modulus, which is a contribution of both a storage modulus and a loss modulus that, respectively, represent stiffness and viscosity (Wirtz, 2009). These two methodologies can be used in biomimetic environments and are appealing as they are used in conjunction with live-imaging microscopy, revealing additional cellular dynamics otherwise lost with end-point assays. However, the use of foreign fluorescent particles embedded within the matrix (TFM) or injected into the cells (PTMR) could have unknown downstream biological effects, or might not be applicable in all systems (e.g. *in vivo* tissues).

Thus, developing efficient non-invasive computational tools, which utilize time-lapse images for identification and characterization of cellular biomechanical characteristics, would be of value to the scientific community. In view of this, we propose a novel computational tool, which takes as input live-imaging datasets, for automated processing and storage of morphological, migratory and biomechanical (viscoelastic) information for groups of cells (Fig. 1). Time-lapse datasets are used as input to conserve and capture the time-dependent response of cells. Changes in cellular dynamics are a consequence of the response to biophysical cues found in the microenvironment, signals in the form of: (1) substrate stiffness, (2) paracrine and autocrine factors, (3) cell–cell interactions, (4) biomechanical forces, and (5) intrinsic cell physiology (Barker et al., 2015; Gajewski et al., 2013; Medema and Vermeulen, 2011). The responsibility of the cell to maintain or adjust cell shape or motility is dependent on cytoskeletal kinetics and requires an exertion of internal cellular forces. The intimate coupling between exogenous and cell-generated forces (Chen, 2008) implies the existence of an opposite external force, calculated through minimization of sum of squared differences (SSD) between images (Modersitzki, 2004; Vural and Frossard, 2013). As there is a point-wise correlation between pixel points in the images and material points of the cell during cellular deformation, movement in

the pixels can be translated into cellular strain. Image morphing aims to bring the SSD to zero, iteratively moving pixels until two consecutive images of the dataset are identical. The minimization of the SSD is interpreted as the force required for pixel displacement (Modersitzki, 2004; Vural and Frossard, 2013). The two variables (force and displacement) are linked using the Navier–Stokes equation for non-rigid viscous fluid flow and the resultant is a strain field (ϵ) (M. Bro-Nielsen, Medical image registration and surgery simulation, PhD thesis, Technical University of Denmark, 1996; I. Yanovsky, Unbiased nonlinear image registration, PhD thesis, University of California, Los Angeles, 2008; Zitová and Flusser, 2003). Iterative time-dependent strain information was innovatively used for mechanical characterization through Kelvin–Voigt fitting, allowing for measures of cellular stiffness (k) and viscosity (η).

In order to apply an image-based program for analysis of cellular biomechanical properties in real-time imaging, the image-morphing algorithm is coupled with the automated cell segmentation and path alignment program (CSPA, available at <https://figshare.com/s/a207830096d7cdd32164>, see Data Availability section for details), the latter yielding migration trajectories and cell boundary data to provide single-cell characterization from multi-cell images. The outcome of this is high-throughput analysis, currently not possible in experimental techniques for biomechanical assessment of cells.

RESULTS

We demonstrated the capabilities of our approach by analyzing temporal differences between: (1) cells of different lineage, human mesenchymal stem cells (huMSCs) before and after (huOBs) exposure to osteoinduction conditions; and (2) cells of different phenotype, collagen-encapsulated naïve CD8⁺ T-lymphocytes (T cells) and T cells stimulated with phorbol 12-myristate-13-acetate (PMA) and ionomycin to invoke an immune response.

Multi-criterion path alignment improves automated tracking of live-imaged cells

The performance of the CSPA program was assessed by examining the relationship between automatically extracted and manually obtained data from randomly selected naïve T cell ($n=32$, Fig. 2A) datasets. From the cell migration trajectories, we analyzed mean square displacement (MSD, Fig. 2B–D) as the temporal variable, and cell area information (Fig. 2E–G) as the spatial variable. Corresponding manual and automated MSD values are distributed roughly equally around a 1:1 line of correspondence (Fig. 2C), with an overall average (absolute percent difference) of 2.22% (Fig. 2D; Table S1). Manual segmentation has been shown to, not only underestimate, but also, incorrectly estimate the cell area by omitting the true edge of the cell (Fig. 2F,G; Table S1). The natural three-dimensional form of a cell will place it slightly out of the focal plane as blurry or white, thus the ability of the program to adjust color thresholds yields a more accurate, yet slightly larger, realistic cell area. Although we find the manual estimates of area to be unreliable and inconsistent (Fig. S1), they (manual and auto) are both consistent when measuring area change (ΔA) (Fig. 2E).

Temporal analysis of differentiating huMSCs

We analyzed the temporal changes of huMSC biomechanics (Fig. 3A), migration and morphological (Fig. 3B) parameters in response to osteoinduction treatment, using our computational approach. The huMSC physiological kinematics were analyzed

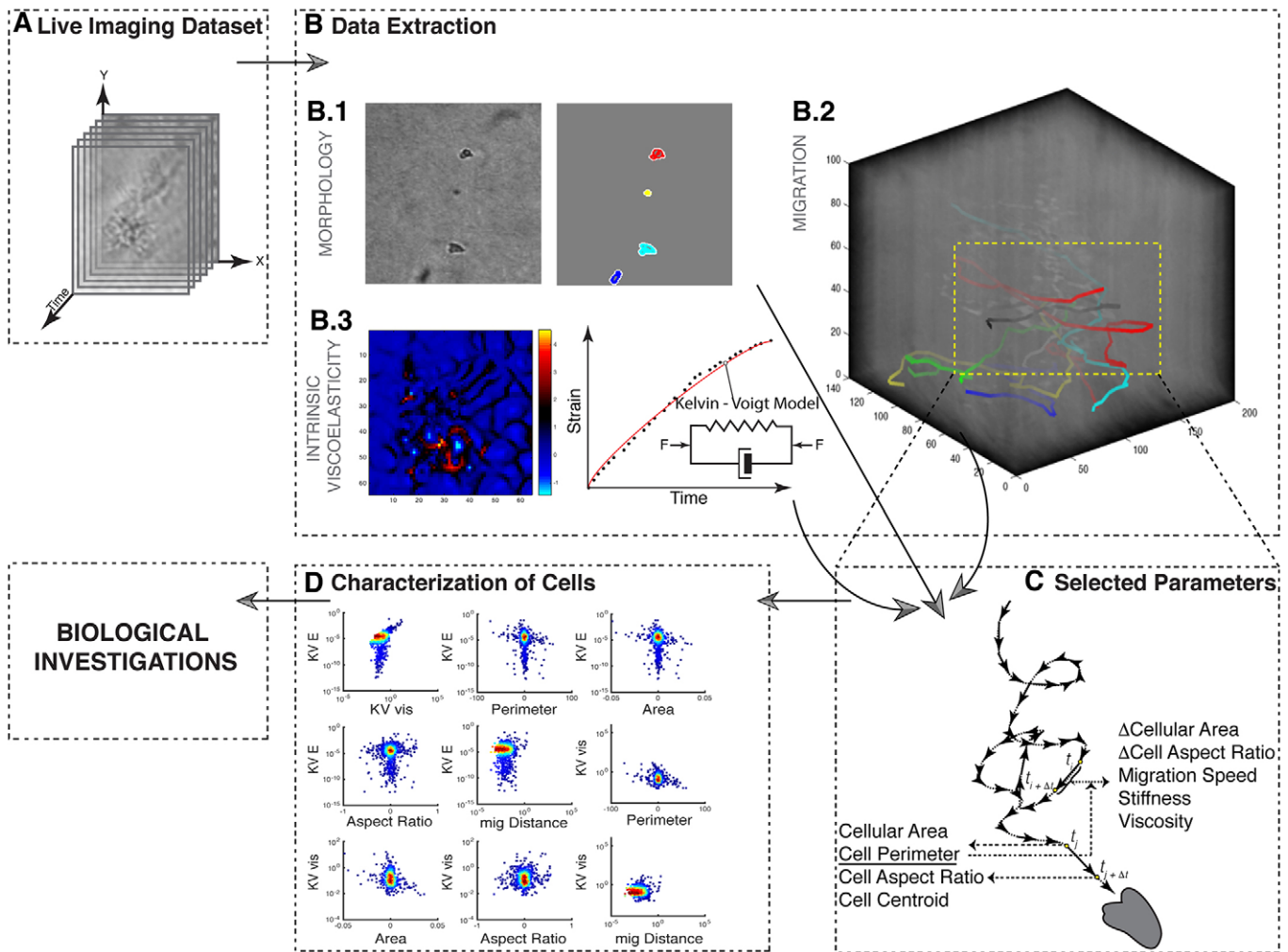


Fig. 1. Comprehensive non-invasive cell characterization. Schematic of the process. (A) First, bright-field images are generated through transmitted light microscopy. (B.1) Time-lapse images are processed and segmented for cell identification, and morphology data extraction and cell perimeters are identified. (B.2) Centroids are compared and aligned based on a multi-criterion algorithm. (B.3) An image-morphing algorithm is applied to pairs of images to generate strain fields, for measuring stiffness and viscosity by fitting to a viscoelastic model. The segmentation process provides perimeter coordinates, used to frame cells, which in turn isolates cellular strain fields produced with image morphing. (C) Output parameters are then analyzed for (D) characterization of cells.

from time-lapse images acquired for 24 h post-seeding, and afterward compared to another similar set of images imaged 5 days after induction towards the osteoblastic lineage (huOB) (Fig. 4). Success of the differentiation was confirmed through the detection of alkaline-phosphatase-positive cells (Fig. 3C). On average, a decrease in cellular stiffness (k) was measured when huMSCs were induced to differentiate into huOBs (Fig. 3A) [$k_{\text{huMSC}}=3.27\pm 0.99$ versus $k_{\text{huOB}}=3.18\pm 0.64$ ($\times 10^{-4}$ Pa)]. Furthermore, we measured a corresponding increase in viscosity [$\eta_{\text{huMSC}}=3.31\pm 0.31$ versus $\eta_{\text{huOB}}=4.82\pm 0.33$ ($\times 10^{-1}$ Pa s)] (results are mean \pm s.e.m., Fig. 3A). Osteoinduced huMSCs also showed decreased average migration speeds [$v_{\text{huMSC}}=2.83\pm 0.38$ versus $v_{\text{huOB}}=2.29\pm 0.35$ ($\times 10^{-2}$ μm 15 min^{-1})], and morphologically a slight increase in change in cellular area [$\Delta A_{\text{huMSC}}=1.28\pm 1.80$ versus $\Delta A_{\text{huOB}}=1.32\pm 1.93$ ($\times 10^{-4}$ μm^2)] (Fig. 3B) and declination in the change in aspect ratio [$\Delta \text{AR}_{\text{huMSC}}=2.29\pm 4.49$ versus $\Delta \text{AR}_{\text{huOB}}=0.53\pm 5.84$ ($\times 10^{-3}$)]. Through comparison of scatter color density plot distributions of temporal parameters of huMSCs (Fig. 4A) and huOBs (Fig. 4B), we further revealed an emerging cluster of cells after osteoinduction with two distinct sub-populations distinguished by their different viscosity.

Temporal analysis of phenotypically different murine T cells

In contrast to the previous case of analyzing differentiating cells, murine T-lymphocytes (hereafter T cells) embedded in collagen I matrices examined with our developed computational tool, revealed more distinct migratory, morphological and biomechanical differences when comparing naïve to PMA/Iono-stimulated T cells (Figs 5 and 6). Not only was there a measured increase in T cell stiffness upon stimulation [$k_{\text{naïve}}=1.02\pm 0.33$ versus $k_{\text{stimulated}}=2.30\pm 0.29$ ($\times 10^{-3}$ Pa)] (results are mean \pm s.e.m., Fig. 5A), our findings further show that stimulated T cells dwell spatially for periods of time, evident through decrease in migration speeds [$v_{\text{naïve}}=11.08\pm 0.83$ versus $v_{\text{stimulated}}=4.49\pm 0.37$ (μm 1.5 min^{-1})] (Fig. 5B), from migration path visualization (Fig. 5C), and quantified by ensemble mean squared displacement [$\text{MSD}_{\text{naïve}}=6555.36$ versus $\text{MSD}_{\text{stimulated}}=2128.95$ (μm^2)] analysis (Fig. 5D). The low viscosity of naïve T cells increases after PMA and ionomycin stimulation [$\eta_{\text{naïve}}=7.90\pm 0.77$ versus $\eta_{\text{stimulated}}=14.08\pm 0.56$ ($\times 10^{-2}$ Pa s)]. Calculated absolute ΔA was lower for the case of stimulated T cells [$\Delta A_{\text{naïve}}=1.66\pm 2.21$ versus $\Delta A_{\text{stimulated}}=5.37\pm 1.54$ (μm^2)], as with their change in aspect ratio [$\Delta \text{AR}_{\text{naïve}}=2.17\pm 5.85$ versus $\Delta \text{AR}_{\text{stimulated}}=6.11\pm 4.28$ ($\times 10^{-3}$)]

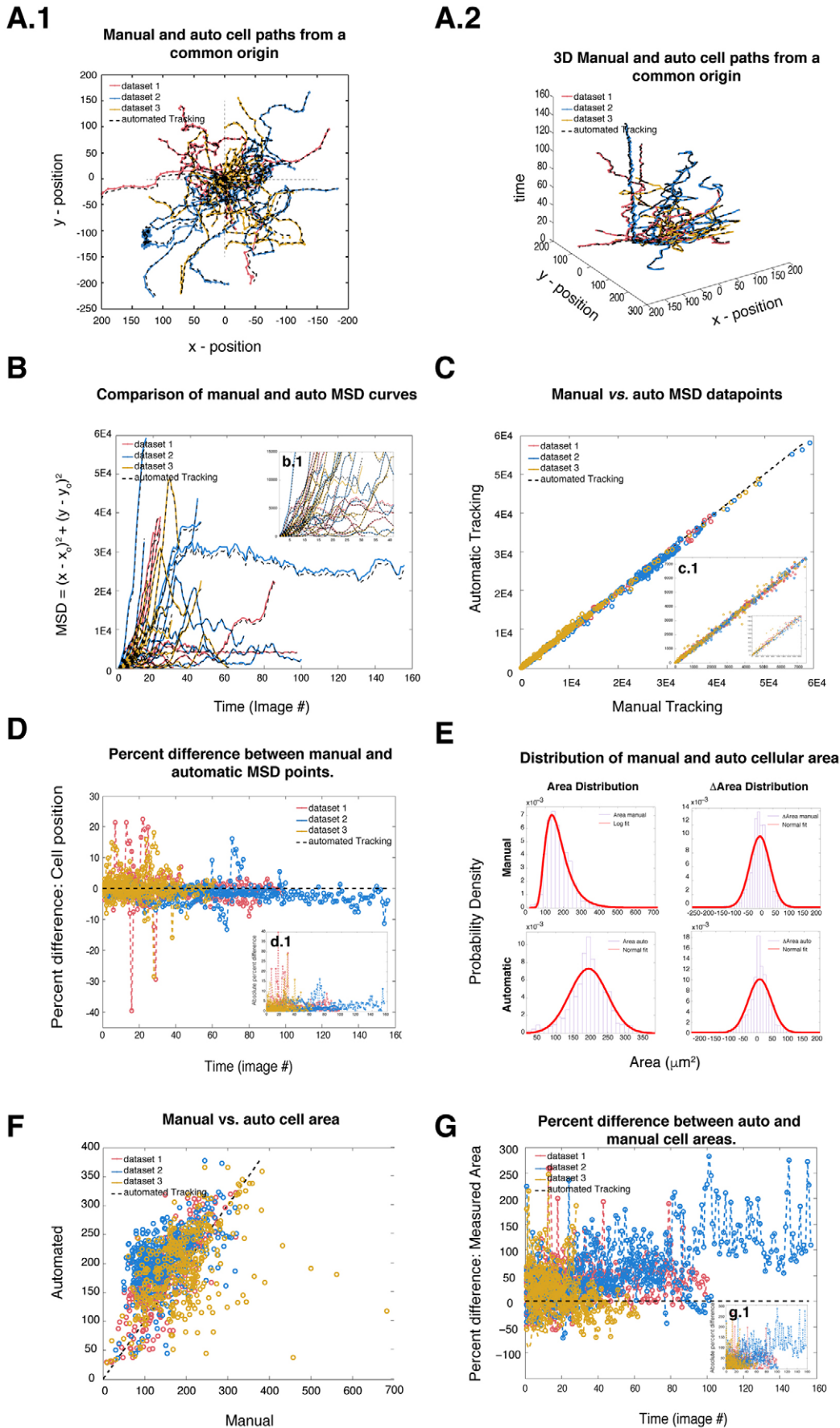


Fig. 2. See next page for legend.

Fig. 2. Temporal and spatial assessment of CSPA. (A) Comparison of manually (solid lines) and automatically (dashed lines) obtained T cell paths (32 individual trajectories from three separate datasets) are shown in two and three dimensions. (B) Corresponding manual (MSD_m) and automated (MSD_a) MSD values (C) are distributed roughly equally around a 1:1 line of correspondence. (D) Percent difference between MSD_m and MSD_a is 2.22% on average, indicating that centroids are well-measured with either method (see Table S1). (E) Best fit distributions of measured area are not consistent when comparing manual (A_m) to automated (A_a) values, despite the distribution of area change (ΔA_m and ΔA_a) being consistent. (F) Plot of A_m and A_a , and (G) percent differences display a consistently higher A_a . This indicates that manually measured areas are unreliable and inaccurate. The improved consistency in area estimation by automated measurements can clearly be seen by eye (see Fig. S1).

(Fig. 6A). A shift in the scatter color density plot distributions of the temporal parameters is apparent after PMA and ionomycin stimulation, revealing linear correlations between $\eta_{stimulated}$ and $\Delta A_{stimulated}$, $\eta_{stimulated}$ and $\Delta AR_{stimulated}$, and $k_{stimulated}$ and $\Delta A_{stimulated}$ (Fig. 6B).

DISCUSSION

We have developed a computational platform that couples two modular programs, one automatically extracting migratory and morphological information of cells, and the other measuring cellular viscoelastic properties from live-imaging datasets. Together, the programs are a non-invasive and label-free tool which we validate and demonstrate the capabilities of by testing on two case studies: (1) distinguishing stem cells and stem cells differentiated into the distinct osteoblastic lineage, and (2) naïve T cells and stimulated T cells, which provide a biomimetic example different from the huMSC model, with increased migratory and morphologic dynamics. Mechanical parameters of the cells are compared by first measuring changes in relative stiffness differences in differentiated and undifferentiated stem cells, and compared to results found with AFM studies. Furthermore, we distinguished naïve from stimulated T cells with expected characteristics necessary to invoke immune response. Interestingly, we detected increased viscoelasticity, decreased random migration and morphologic behavior from stimulated T cells as compared to naïve T cells. These changes in behavior are consistent with newly acquired functional requirements of stimulated T cells as an effector arm of the immune response in peripheral tissue.

In reference to cell (or particle) tracking, a number of algorithms and tools have been proposed for both semi-automated and automated segmentation and tracking of (labeled) cells (Lamprecht et al., 2007; Li et al., 2008; Miura, 2005). However, a one-size-fits-all segmentation and cell tracking program has yet to be established. We found that for the case of unlabeled (i.e. without fluorescent staining of the nucleus or cytoplasm) multi-object tracking, there are only few programs available (Hand et al., 2009; Huth et al., 2010). Of those available, even fewer can segment and track multiple-fast moving and unlabeled cells; thus, such approaches typically require customized programmable criteria to meet the needs of a specific goal. For this study in particular, we had several objectives that needed to be met (requiring in-house customization): (1) to accurately segment multiple cell boundaries in each bright-field image, (2) store both the centroids and area for each cell in each image, (3) link each cell in each image with itself in subsequent images, and (4) extract cell boundaries, which is the link to part two of our platform. There were some obstacles specific to our datasets: first, cells moved fast, often entering and exiting the focal plane; second, cell paths were hard to accurately align based on commonly used nearest neighbor algorithms alone, mainly due to

interference of other cells in the vicinity (J.-Y. Tinevez, Simple Tracker, MATLAB File Exch, 2012). The two mentioned issues cause cell paths to be substantially shorter (by ~66%, i.e. tracked for short time frame when compared to manual) and either a new disjoint path would form or cell paths would jump tracks, continuing along the path of another cell (see Fig. S2). For the case of CSPA, we found that the inclusion of multi-criteria path alignment feature significantly improved the accuracy of detected cell paths: cells were tracked for their time duration within the focal plane and cells did not jump tracks with the inclusion of minimizing spatial shape change (per cell) across frames.

The use of image morphing to acquire mechanical characteristics is novel and expected to be applicable to a wide range of biological investigations. The algorithm captures cellular stiffness and viscosity, which can be used for relative comparison against appropriate controls. Traditional mechanical testing measures the deformation of an object when subjected to a known applied force, here forces are approximated from images instead. Time-lapse images have been used successfully in estimating forces in a wide array of fields, including vision object detection, robotics and satellite imagery, applications where direct measurements of deformations are not possible (Jagannathan et al., 2011). The external applied force that deforms the cells is treated as an opposing force to outward exertion of internally generated forces (detailed in the User Guide Section 3.1 available at <https://figshare.com/s/a207830096d7cdd32164>). This coupling between exogenous and endogenous-cell-generated forces is simply described by Newton's 3rd Law and further justified through detailed mechanotransduction (Chen, 2008) principles. The image similarity measure is taken as the driving force of the morphing process (Modersitzki, 2004), the applied force field required to morph (transform) one image onto another; analogous to the force required to deform an object from one shape (deformation) to another. Image morphing is approached through minimizing the similarity measure (SSD) between two images (Modersitzki, 2004; Vural and Frossard, 2013). We calculated force fields from detectable changes in intensity values of consecutive image pairs; this takes into account both the shape of the cell as well as information within the cytosolic region. It should be noted that peripheral shape alone has been reported to be sufficient in predicting magnitude and direction of cell-generated forces (Lemmon and Romer, 2010).

The magnitude of the image-based force approximations is solely dependent on imaged cellular deformation, which could be influenced by other factors such as the stiffness of the substrate. Indeed this is the case, as the said digitally measured mechanical properties of cells is a function of the local microenvironment over time and not a single absolute value assumed by experimental techniques. For the case of absolute measures, for example, to optimize stem cell differentiation protocols, an image movement to force calibration should be performed when possible. Our method is suited to evaluate relative changes; we verified that an increase in physical force differs from image-based force approximation by a simple scaling factor (detailed in User Guide Section 3.4).

The number of studies using AFM to quantify huMSC and huOB stiffness allowed us to then gauge the biomechanical properties measured using the image-morphing algorithm (Bongiorno et al., 2014; Darling et al., 2008; Docheva et al., 2008; Titushkin and Cho, 2007; Yourek et al., 2007). Our measurements showed a drop in cellular stiffness after huMSCs were induced to differentiate into huOBs, an observation that is likely linked to the decline in both cytoskeletal actin thickness and order in osteoblasts as reported by studies using fluorescent imaging of phalloidin-stained cells

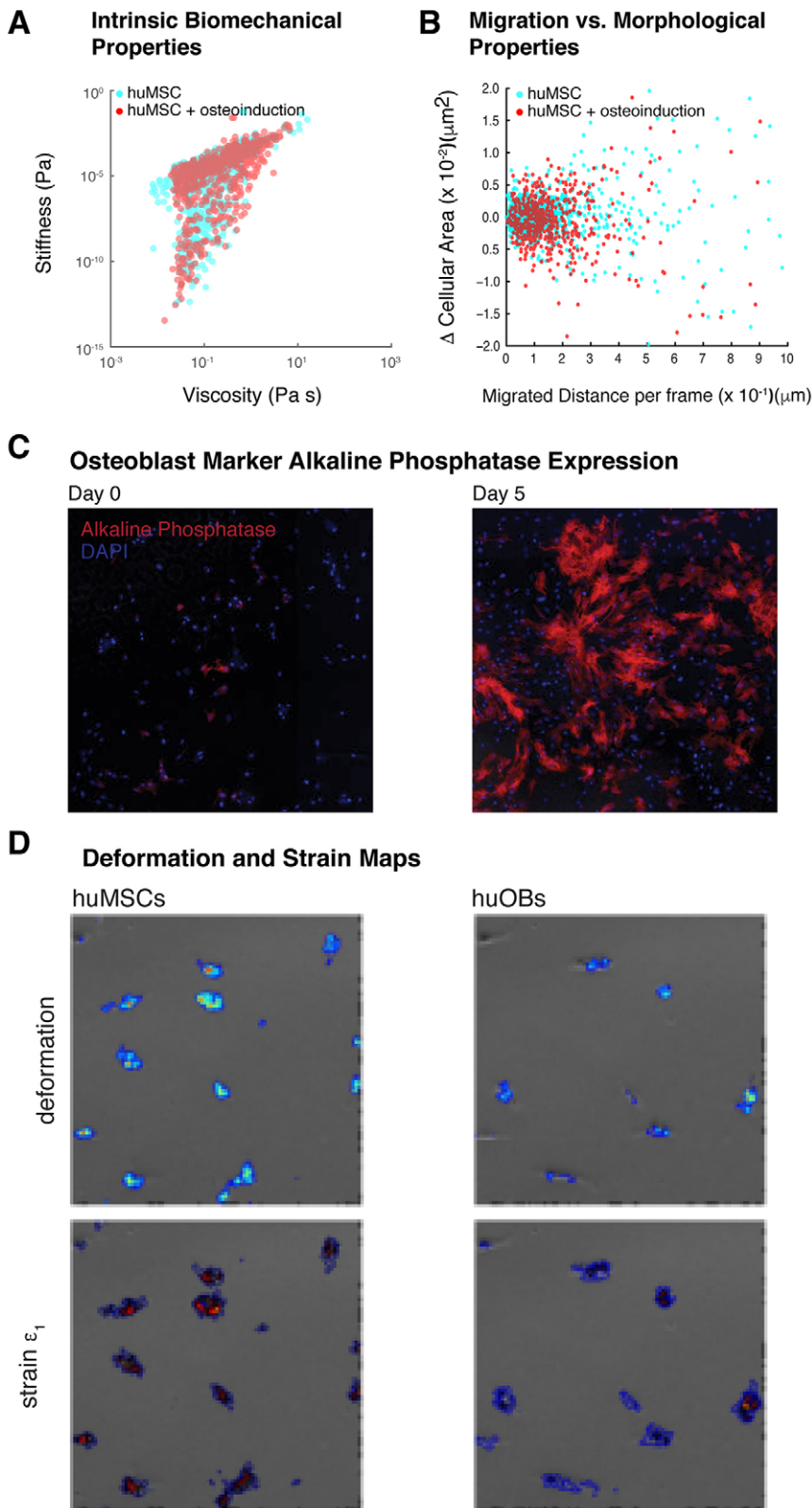


Fig. 3. Comparative characterization of huMSCs differentiated towards huOBs. (A) We measured an overall decrease in temporal stiffness [$k_{\text{huMSC}}=3.27 \pm 0.99$ versus $k_{\text{huOB}}=3.18 \pm 0.64$ ($\times 10^{-4}$ Pa)], and the resultant $k_{\text{huOB}}/k_{\text{huMSC}}$ ratio was within the reported range from researchers using AFM (Table S2). (B) Additionally, huOBs have decreased migration velocities [$v_{\text{huMSC}}=2.83 \pm 0.38$ versus $v_{\text{huOB}}=2.29 \pm 0.35$ ($\times 10^{-2}$ μm 15 min^{-1})] and were shown to have a declining area [$\Delta A=-1.28 \pm 1.93$ ($\times 10^{-3}$ μm^2)]. When huMSCs differentiated into (C) alkaline-phosphatase-positive huOBs viscosity increased [$\eta_{\text{huMSC}}=3.31 \pm 0.31$ versus $\eta_{\text{huOB}}=4.82 \pm 0.33$ ($\times 10^{-1}$ Pa s)]. (D) Representative deformation and maximum principle strain maps are shown. In total, the number of huMSCs and huOBs analyzed (90 temporal points per cell; 15-min interval for 24 h) were 28 and 30, respectively. Numerical results are mean \pm s.e.m.

(Titushkin and Cho, 2007; Yourek et al., 2007). Although studies produced similar qualitative actin cytoskeleton changes, they interestingly reported conflicting trends when acquiring k values from huMSCs and huOBs using AFM (Titushkin and Cho, 2007; Yourek et al., 2007), a discrepancy that further emphasizes the present challenges in measurement repeatability and reproducibility

using high-resolution apparatus. Additional evaluation against other studies which also use AFM techniques for stiffness measurements (Table S2) revealed that our resulting huOB to huMSC k ratio of 0.97 ($k_{\text{huOB}}/k_{\text{huMSC}}=0.97$) measured by image morphing was within the documented range of 0.44–2.41 (Bongiorno et al., 2014; Darling et al., 2008; Docheva et al.,

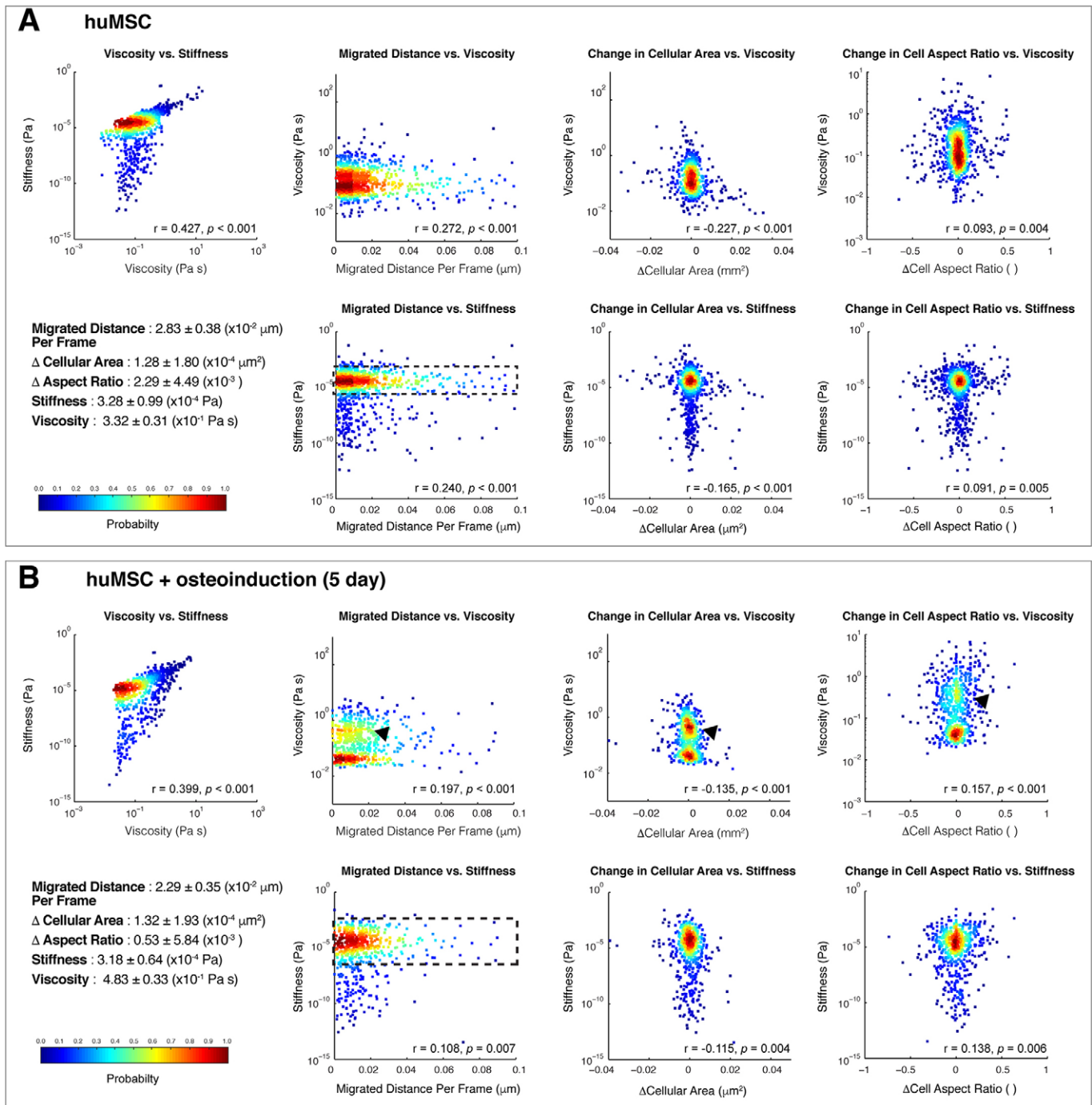


Fig. 4. Probability density plots, correlation and least squares fit of measured biomechanical properties, morphological and migration parameters of osteogenically differentiated huMSCs. (A) huMSCs are induced to differentiate into (B) huOBs. Significant ($P < 0.001$, P -values are derived from Student's t distribution), but weak, correlations between stiffness and viscosity, and viscosity versus migration distance and area change (ΔA) exist. There is, however, a clear change in viscosity as huMSCs differentiate into huOBs: two distinct distributions of viscosity emerge (B, top row, arrowheads). There is no visible change in measured cell stiffness, but a difference in data spread is apparent as huMSCs ($n=28$) differentiate into huOBs ($n=30$) (A and B, bottom row, dashed boxes). The qualitative differences in the density plot before and after differentiation are quantified through changes in statistical correlation results. It is interesting to note that the probability density plot (representing the majority of cells) displayed a single viscosity peak at $\sim 10^{-1}$ Pa s (A, row 1, panels 2, 3, 4). However, after being osteoinduced for 5 days, the viscosity splits into two distinct groups at $\sim 10^{-1}$ and $10^{-1.5}$ Pa s (B, row 1, panels 2, 3, 4). Numerical results are mean \pm s.e.m.

2008; Titushkin and Cho, 2007; Yourek et al., 2007). Stiffness calculated from experimental force-deformation studies, such as AFM, have been reported to be difficult to interpret (Janmey and McCulloch, 2007). Large variation in collected data, despite having reproducible results, is attributed to intracellular heterogeneity. Moreover, cytoskeletal composition, its associated proteins, and

other cellular components fluctuate with respect to space and time, which is an additional characteristic that our platform is able to capture. Furthermore, CSPA detected a decrease in migratory capacity and morphological changes after osteoinduction, similar to that reported by Ichida et al. (2011). We further emphasize that computational image-morphing techniques as we report here can be

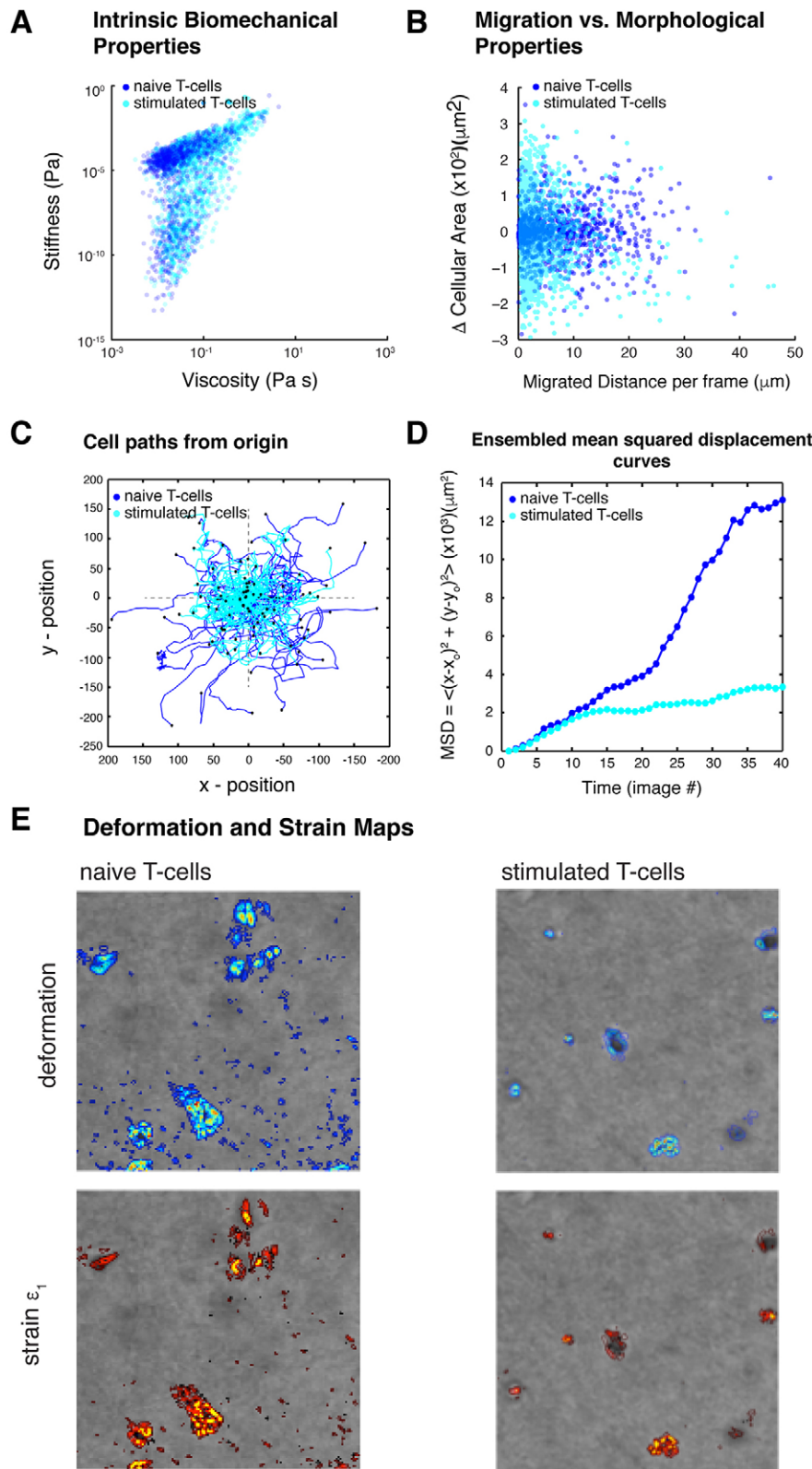


Fig. 5. Comparative characterization of naive, and PMA- and ionomycin-stimulated murine CD8⁺ T cells. (A) Stimulated T cells have increased stiffness [$k_{\text{naive}}=1.02\pm 0.33$ versus $k_{\text{stimulated}}=2.30\pm 0.29$ ($\times 10^{-3}$ Pa)] and viscosity [$\eta_{\text{naive}}=7.90\pm 0.77$ vs $\eta_{\text{stimulated}}=14.08\pm 0.56$ ($\times 10^{-2}$ Pa s)] when compared to naive, unstimulated controls. (B) Migration velocity slowed down after stimulation [$v_{\text{naive}}=11.08\pm 0.83$ vs $v_{\text{stimulated}}=4.49\pm 0.37$ ($\mu\text{m } 1.5 \text{ min}^{-1}$)] with an increased change in area [$\Delta A_{\text{naive}}=1.66\pm 2.21$ vs $\Delta A_{\text{stimulated}}=5.37\pm 1.54$ (μm^2)]. (C) Naive T cells surveyed a broader surrounding area, of (D) ~ 3.08 -fold more based on ensemble mean square displacement plots. (E) Representative deformation and maximum principle strain maps are also shown. In total the number of naive and stimulated T cells analyzed (80 temporal points per cell, 1.5 min interval for 2 h) were 49 and 39, respectively. Numerical results are mean \pm s.e.m.

used in general as a label-free marker to distinguish cells in culture. Illustrating this, through intracellular deformation and corresponding strain fields, is the observation of a more homogenous population of cells prior to osteoinduction (Fig. 3D), signifying that differentiation into the osteoblastic lineage is non-uniform.

Current evidence supports the hypothesis that robust T cell activation and function is dependent upon mechanotransduction pathways initiated at the immunological synapse (Comrie et al., 2015; Xie et al., 2012), however, very little is known about lymphocyte sensing of biophysical properties within peripheral tissues. Although naive T cells are activated in cell-dense lymphoid

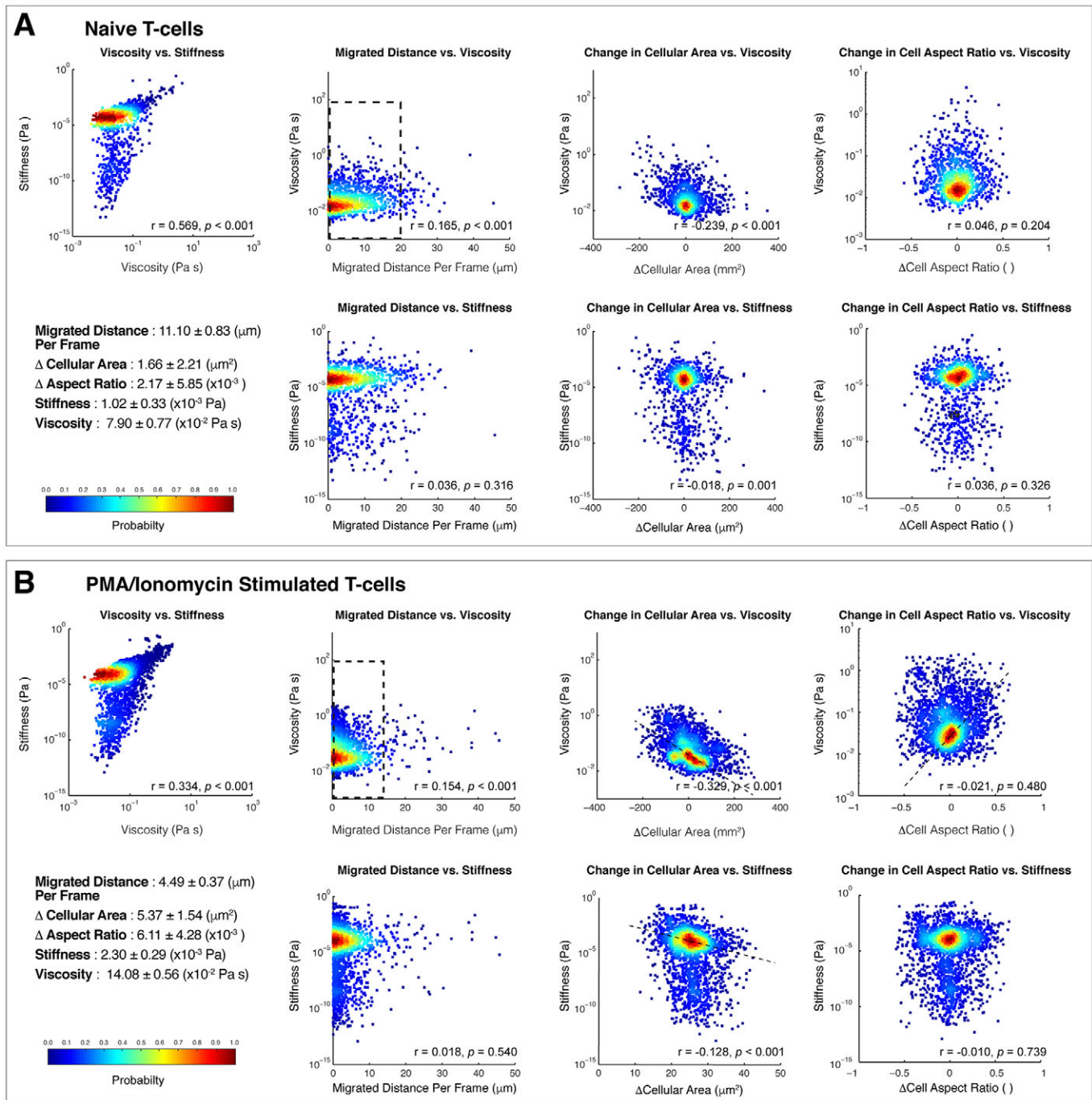


Fig. 6. Probability density plots, correlation, and least squares fit of measured biomechanical properties, morphological, and migration parameters of naïve, and PMA- and ionomycin-stimulated CD8⁺ T cells. Analysis of computer model output for (A) naïve murine T cells ($n=49$) and (B) PMA- and ionomycin-stimulated T cells ($n=39$). Significant ($P < 0.001$, P -values are derived from Student's t distribution), but weak, correlations between stiffness and viscosity, and viscosity versus area change (ΔA) and migration distance exist. Correlation increases after activation, and the emergence of spread in cell ΔA is evident (B) and migration distances decrease (A and B, dashed boxes). The measured stiffness, viscosity, ΔA and ΔAR distributions broaden when T cells are stimulated. Numerical results are mean \pm s.e.m.

organs where collagen fibers are encased in fibroblastic reticular cells, they function within protein-rich peripheral tissues (Nourshargh et al., 2010). Integrins, and downstream cytoskeletal machinery, are required for lymphocyte extravasation and interstitial migration through inflamed peripheral tissue (Overstreet et al., 2013), and T cells are found in close association with matrix fibers in skin, brain and tumors (Boissonnas et al., 2007; Mrass et al., 2006; Wilson et al., 2009). The distinct extracellular biophysical properties

at sites of T cell activation and function indicate that T cells themselves acquire distinct, intrinsic biophysical properties to enable migration and function within these microenvironments. Consistent with this hypothesis, we measured an increased stiffness of activated T cells as compared to their naïve counterparts when stimulated with PMA and ionomycin in type I collagen gels (Fig. 5A; Movie 1). The altered cellular viscosity correlated with increased dwell times in gels as well as decreased migration velocities (Fig. 5B). Literature

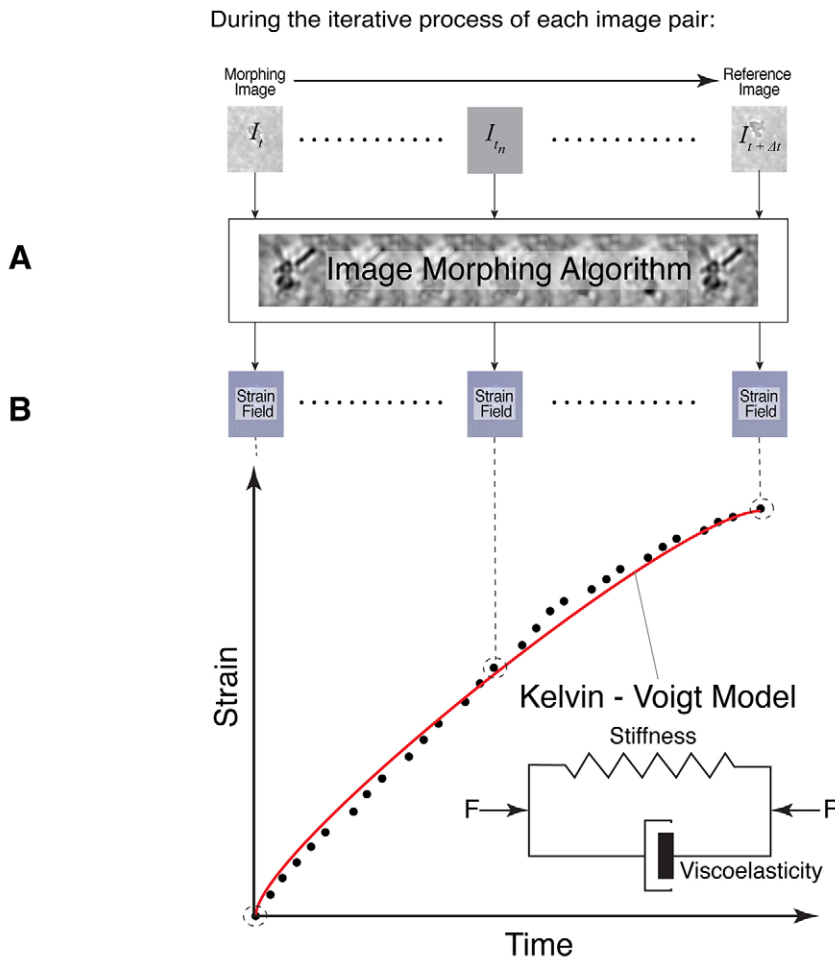
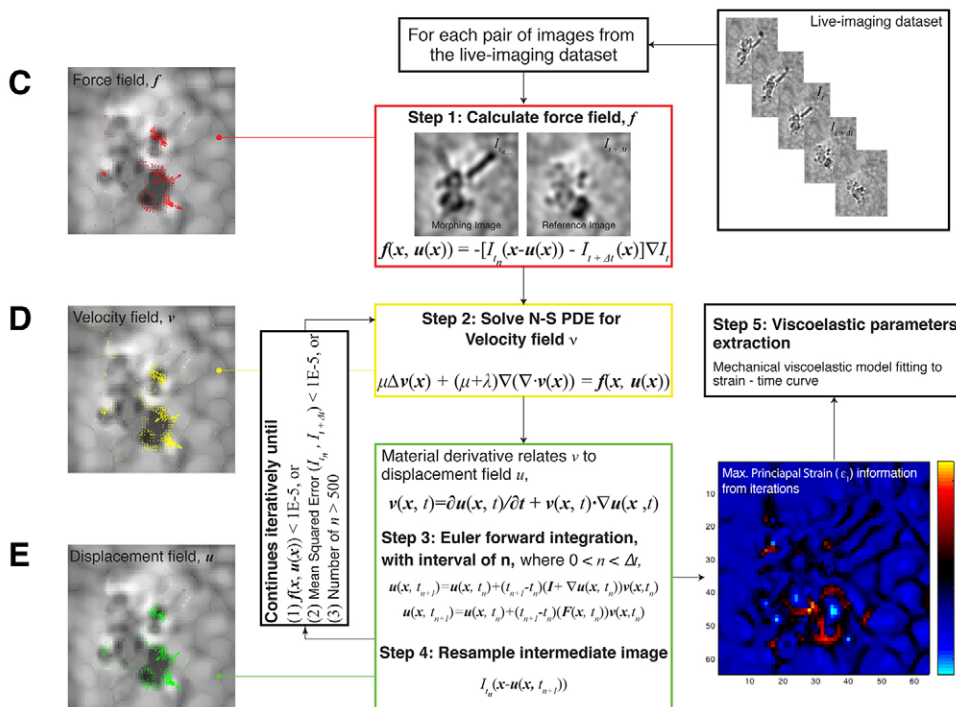


Fig. 8. Extraction of intrinsic cellular viscoelastic properties. (A) Iterative strain information is captured through the morphing process. (B) Extracted average maximum principle strain versus time data are fitted to a Kelvin–Voigt viscoelastic model to determine intracellular biomechanical properties. (C) Force fields are calculated based on image differences, and (D) used as input to a viscoelastic Navier–Stoke equation to determine velocity fields. (E) Finally, the material derivative yields a related displacement field from which we can obtain an Almansi strain tensor, yielding comprehensive strain information for the cell(s).

Image Morphing Algorithm:



biologically based mathematical modeling framework. This will facilitate steady data streaming for applications such as cell sorting systems, stem cell fate prediction, and assessment of tissue engineering construct prior to translational therapies, all without compromising the integrity of the biological system.

MATERIALS AND METHODS

Cell differentiating assay

Primary human adult mesenchymal stem cells (huMSCs) were obtained from Lonza (Basel, Switzerland) and cultured according to the manufacturer’s instructions and utilized to determine the feasibility of measuring differences in differentiating cells. huMSCs were seeded at a density of 500 cells cm⁻² on type I collagen (Sigma Aldrich, St Louis, MO) tissue culture plates. Phase-contrast images were acquired at 15-min intervals for 24 h using a customized imaging microscope (ImageIQ Inc., Cleveland, OH) before and 5 days after osteoinduction. The imaging microscope maintained ambient cell culture conditions (37°C and 5% CO₂). Osteogenic induction was performed using a StemPro(R) Osteogenesis Differentiation Kit (Gibco, Life Technologies, Carlsbad, CA) according to the manufacturer’s instruction. At day 6, after live imaging, osteoblast differentiation was detected by alkaline phosphatase expression.

Cell phenotypic assay

We measured and compared different phenotypes of CD8⁺ murine T-lymphocytes (T cells). Naïve CD8⁺ T cells from C57BL/6 mice were isolated by magnetic sorting (negative CD8 sort, EasySep Stem Cell Technologies) and embedded into 1.5 mg ml⁻¹ type I collagen (Advanced Biomatrix Inc., Carlsbad, CA) at a density of 25,000 cells ml⁻¹. Following gel formation, naïve CD8⁺ T cells were either left untreated or stimulated with 10 ng ml⁻¹ phorbol 12-myristate-13-acetate (PMA) and 1 µg ml⁻¹ ionomycin (Sigma, St. Louis, MO). Cells were imaged at 1.5-min intervals for 2 h using a commercial phase-contrast inverted microscope (Axiovert 200, Carl Zeiss Microscopy GmbH, Munich, Germany) equipped with an enclosed incubation system (Incubation System S, PeCon GmbH) to maintain physiological ambient conditions. All animal experiments were conducted in accordance with approval from the Cantonal Veterinary Office of Canton de Vaud, Switzerland according to Swiss Law.

Computational programs

The image processing programs (1) for image morphing and (2) for cell segmentation path alignment (CSPA) were developed in MATLAB (The MathWorks Inc., Natick, MA) as a modular program, each capable of independent usage. The programs can be easily adapted for the analysis of a wide variety of time-lapse data, and the source code is available from <https://figshare.com/s/a207830096d7cdd32164>. Readers are encouraged to refer to the user guide that accompanies this code for detailed explanation of the technique employed.

Automated CSPA

The newly developed CSPA program (Fig. 7) is a user-friendly, highly flexible algorithm designed to analyze phase-contrast time-lapse videos of live-cell dynamics under varied experimental conditions to extract migration and time-variant morphological parameters (Fig. S3). The program follows a sequence of logical steps: objects within each image are identified through erosion with a structuring element, followed by adaptive thresholding and subsequent noise removal (Fig. 7A).

Cell identification and alignment occurs through consecutive image comparisons, where all cells are measured against each other, through their displacement and shape fluctuation, measured by the magnitude of area change (ΔA) (Fig. 7B.1). Top-down and bottom-up data scanning is designed to allocate the indices of optimal combinations of cells using the criteria of minimum movement and subsequent minimum ΔA (Fig. 7B.2). Following this process, cells are treated as ‘old’ if matched or ‘new’ if unmatched (Fig. 7B.2). Objects appear or disappear from the field of view during the course of the image sequence. Moreover, objects also become temporarily occluded from the field of view. This issue is addressed with an additional customized data mapping option. An ‘old’ object implies it will

align with an already-initialized path in one of two ways: (1) direct mapping with itself in the previous (*t*−Δ*t*) image; or (2) mapping to itself in the *t*−*n*×Δ*t* (where *n* is the image number) image; for this case, a customized data mapping scheme is required. Unmatched objects are tested against the closest prior image with at least as many objects as the current image, if the two (distance and area) criteria are met, the current unmatched object will link with the path of the matched cell. An object identified as ‘new’ will initialize a new cell path. All indices are systematically stored and used for data storage for subsequent analysis of time-dependent cell properties (Fig. 7C). As a measure of algorithm performance, randomly selected naïve T cells were manually tracked using ImageJ (Schneider et al., 2012) for comparisons with their automated counterparts. For each live-imaging dataset with time interval (Δ*t*), each sequential position *p*_{*t*} (*x*_{*t*}, *y*_{*t*}) of each cell of interest is calculated as the center of mass, found by clicking on a mouse and tracing the outline (perimeter) of the cell (Fig. S1). Automated tracking algorithms took an average of 0.12 (0.06) min per dataset; manual tracking alone took on average 12.57 (12.32) min (the numbers in brackets refer to the s.d.). Manual tracking of individual cells can take between 1.50 min and 55.20 min, tracking identical cells using CSPA takes between 3.13 s up to a maximum of 14.04 s, a 99% decrease in time (Table S3).

Measuring cell biomechanics through image morphing

Cell shape is never constant. Cell migration and dendrite extensions present the most drastic change in morphology, which exhibit flow and squeezing-like characteristics during these processes. To capture the relatively large complex displacements during shape change, we adopted a non-rigid viscous fluid flow registration approach (Bro-Nielsen and Gramkow, 1996; D’Agostino et al., 2003; Zitová and Flusser, 2003) (Fig. 8), also known as image morphing (Fig. S2). Sequential pairs of images are denoted *M*(*x*)_{*t*} and *S*(*x*)_{*t*+Δ*t*}, where *M*(*x*) is the moving image that is morphed into *S*(*x*), the static image (Movie 2a). The morphing process determines a displacement field *u*(*x*) so that the difference between *M*(*x*−*u*(*x*)) and *S*(*x*) is minimized or equal to zero. This displacement is dependent on the balance of forces within the fluid as determined by the Navier–Stokes partial differential equation for compressible viscous fluids using the Eulerian reference frame:

$$\Delta v(x) + \nabla(\nabla \cdot v(x)) = f(x, u(x)), \tag{1}$$

where *v*(*x*) is the velocity field, *f*(*x*, *u*(*x*)) is the force field that is used to drive the viscous flow; here, we define *f*(*x*, *u*(*x*)) as derivative of the sum of squared difference between the images (Modersitzki, 2004; Vural and Frossard, 2013):

$$f(x, u(x)) = -[M(x - u(x, t)) - S(x)]\nabla M|_{x=u(x, t)}. \tag{2}$$

Eqn (1) is solved for *v*(*x*, *t*) using the force field obtained from Eqn (2), and the corresponding displacement field *u*(*x*, *t*) can be calculated using the material derivative, Eqn (3), a time rate change of a property on a particle in the a velocity field, in this case displacement:

$$v(x, t) = \frac{\partial u(x, t)}{\partial t} + v(x, t) \cdot \nabla u(x, t). \tag{3}$$

A forward finite difference approach, with iterative time interval *n*, is used to extract an estimate of the time derivative Eqn (4):

$$u(x, t_{n+1}) = u(x, t_n) + (t_{n+1} - t_n)[I + \nabla u(x, t_n)]v(x, t_n) = u(x, t_n) + (t_{n+1} - t_n)[F(x, t_n)]v(x, t_n). \tag{4}$$

This resultant displacement field is applied to *M*(*x*, *t_n*) to yield *M*(*x*, *t_{n+1}*) through image interpolation, this sequence of calculation continues until *f*(*x*, *u*(*x*, *t*)) or the mean squared error between *M*(*x*, *t_n*) and *S*(*x*) is below a user-allowable tolerance. The finite strain theorem allows Euler–Almansi strain tensors to be obtained from the deformation gradient:

$$e(x, t_n) = 0.5[I - F(x, t_n)^{-T}F(x, t_n)^{-1}], \tag{5}$$

where *I* is the identity matrix and the strain components are as follows, *e*(*x*, *t_n*)=[*e*_{*xx*}(*x*, *t_n*) *e*_{*xy*}(*x*, *t_n*);*e*_{*yx*}(*x*, *t_n*) *e*_{*yy*}(*x*, *t_n*)]. The iterative process calculates a temporal average strain field from principal strains, ε₁ and ε₂ (Movie 2b,c).

From this, we derive parameters of viscoelasticity by fitting the Kelvin–Voigt viscoelastic mechanical model (Ekpenyong et al., 2012; Lim et al., 2006). We observed the presence of pericellular noise when implementing the image-morphing program on cells embedded in 3D collagen gels, where cellular forces pull on collagen fibrils creating micro motion. We tackle this issue by calling the CSPA program for automated cell perimeter coordinates (Fig. 7B), for use as a mask in the extraction of strain information.

Statistics

Reported measurements are in the form of mean±s.e.m. Relationships between output parameters were assessed and strength is indicated by the Pearson's linear correlation coefficient (*r*); the significance of the relationship is expressed by probability levels (*P*-value).

Acknowledgements

We thank Dr Matthew N. Martin for his valuable input and critical reading of the manuscript, and Ms Noaf Alwahab, Dr Nicolas Christoforou, and Dr Abdel Isakovic for useful discussions.

Competing interests

The authors declare no competing or financial interests.

Author contributions

Y.E.P. and J.C.M.T. conceived, developed, implemented and analyzed the data output of CSPA and image-morphing programs respectively, together both authors wrote the paper. C.P.N. and J.C.M.T. designed the huMSC study and collected the data. A.W.L. and J.C.M.T. designed the T cell study and collected the data. All authors contributed to the application of algorithms, manual data collection and review of the manuscript. D.L.G. edited the manuscript.

Funding

This manuscript was made possible through Khalifa University of Science, Technology and Research internal research funds [grant number KUIRF 210034]; and the Al Jaila Foundation [grant number AJF201407].

Data availability

A comprehensive user guide for both CSPA and image morphing with a tutorial and detailed explanation of the model and algorithms, together with the MATLAB source code is available for download here: <https://figshare.com/s/a207830096d7cdd32164>

Supplementary information

Supplementary information available online at <http://jcs.biologists.org/lookup/doi/10.1242/jcs.191205.supplemental>

References

- Baker, E. L., Lu, J., Yu, D., Bonneau, R. T. and Zaman, M. H. (2010). Cancer cell stiffness: integrated roles of three-dimensional matrix stiffness and transforming potential. *Biophys J.* **99**, 2048–2057.
- Barker, H. E., Paget, J. T. E., Khan, A. A. and Harrington, K. J. (2015). The tumour microenvironment after radiotherapy: mechanisms of resistance and recurrence. *Nat. Rev. Cancer* **15**, 409–425.
- Bartalena, G., Grieder, R., Sharma, R. I., Zambelli, T., Muff, R. and Snedeker, J. G. (2011). A novel method for assessing adherent single-cell stiffness in tension: design and testing of a substrate-based live cell functional imaging device. *Biomed. Microdevices* **13**, 291–301.
- Bezanilla, M., Gladfelter, A. S., Kovar, D. R. and Lee, W.-L. (2015). Cytoskeletal dynamics: a view from the membrane. *J. Cell Biol.* **209**, 329–337.
- Boissonnas, A., Fetter, L., Zeelenberg, I. S., Hugues, S. and Amigorena, S. (2007). In vivo imaging of cytotoxic T cell infiltration and elimination of a solid tumor. *J. Exp. Med.* **204**, 345–356.
- Bongiorno, T., Kazlow, J., Mezenzev, R., Griffiths, S., Olivares-Navarrete, R., McDonald, J. F., Schwartz, Z., Boyan, B. D., McDevitt, T. C. and Sulchek, T. (2014). Mechanical stiffness as an improved single-cell indicator of osteoblastic human mesenchymal stem cell differentiation. *J. Biomech.* **47**, 2197–2204.
- Bro-Nielsen, M. and Gramkow, C. (1996). Fast fluid registration of medical images. In *Visualization in Biomedical Computing*. 4th International Conference, pp. 267–276. Springer-Verlag London, UK.
- Chen, C. S. (2008). Mechanotransduction - a field pulling together? *J. Cell Sci.* **121**, 3285–3292.
- Comrie, W. A., Li, S., Boyle, S. and Burkhardt, J. K. (2015). The dendritic cell cytoskeleton promotes T cell adhesion and activation by constraining ICAM-1 mobility. *J. Cell Biol.* **208**, 457–473.
- Cross, S. E., Jin, Y.-S., Rao, J. and Gimzewski, J. K. (2007). Nanomechanical analysis of cells from cancer patients. *Nat. Nanotechnol.* **2**, 780–783.
- D'Agostino, E., Maes, F., Vandermeulen, D. and Suetens, P. (2003). A viscous fluid model for multimodal non-rigid image registration using mutual information. *Med. Image Anal.* **7**, 565–575.
- Darling, E. M., Topel, M., Zauscher, S., Vail, T. P. and Guilak, F. (2008). Viscoelastic properties of human mesenchymally-derived stem cells and primary osteoblasts, chondrocytes, and adipocytes. *J. Biomech.* **41**, 454–464.
- Docheva, D., Padula, D., Popov, C., Mutschler, W., Clausen-Schaumann, H. and Schieker, M. (2008). Researching into the cellular shape, volume and elasticity of mesenchymal stem cells, osteoblasts and osteosarcoma cells by atomic force microscopy. *J. Cell. Mol. Med.* **12**, 537–552.
- Ekpenyong, A. E., Whyte, G., Chalut, K., Pagliara, S., Lautenschläger, F., Fiddler, C., Paschke, S., Keyser, U. F., Chilvers, E. R. and Guck, J. (2012). Viscoelastic properties of differentiating blood cells are fate- and function-dependent. *PLoS ONE* **7**, e45237.
- Gajewski, T. F., Schreiber, H. and Fu, Y.-X. (2013). Innate and adaptive immune cells in the tumor microenvironment. *Nat. Immunol.* **14**, 1014–1022.
- Galon, J., Pagès, F., Marincola, F. M., Thurin, M., Trinchieri, G., Fox, B. A., Gajewski, T. F. and Ascierto, P. A. (2012). The immune score as a new possible approach for the classification of cancer. *J. Transl. Med.* **10**, 1.
- Gupta, M., Sarangi, B. R., Deschamps, J., Nematbakhsh, Y., Callan-Jones, A., Margadant, F., Mège, R.-M., Lim, C. T., Voituriez, R. and Ladoux, B. (2015). Adaptive rheology and ordering of cell cytoskeleton govern matrix rigidity sensing. *Nat. Commun.* **6**, 7525.
- Haase, K. and Pelling, A. E. (2015). Investigating cell mechanics with atomic force microscopy. *J. R. Soc. Interface* **12**, 20140970.
- Haessler, U., Pisano, M., Wu, M. and Swartz, M. A. (2011). Dendritic cell chemotaxis in 3D under defined chemokine gradients reveals differential response to ligands CCL21 and CCL19. *Proc. Natl. Acad. Sci. USA* **108**, 5614–5619.
- Haessler, U., Teo, J. C. M., Foretay, D., Renaud, P. and Swartz, M. A. (2012). Migration dynamics of breast cancer cells in a tunable 3D interstitial flow chamber. *Integr. Biol.* **4**, 401.
- Hall, M. S., Long, R., Feng, X., Huang, Y., Hui, C.-Y. and Wu, M. (2013). Toward single cell traction microscopy within 3D collagen matrices. *Exp. Cell Res.* **319**, 2396–2408.
- Hand, A. J., Sun, T., Barber, D. C., Hose, D. R. and MacNeil, S. (2009). Automated tracking of migrating cells in phase-contrast video microscopy sequences using image registration. *J. Microsc.* **234**, 62–79.
- Hoffman, B. D. and Crocker, J. C. (2009). Cell mechanics: dissecting the physical responses of cells to force. *Annu. Rev. Biomed. Eng.* **11**, 259–288.
- Huth, J., Buchholz, M., Kraus, J. M., Schmucker, M., von Wichert, G., Krndija, D., Seufferlein, T., Gress, T. M. and Kestler, H. A. (2010). Significantly improved precision of cell migration analysis in time-lapse video microscopy through use of a fully automated tracking system. *BMC Cell Biol.* **11**, 24.
- Ichida, M., Yui, Y., Yoshioka, K., Tanaka, T., Wakamatsu, T., Yoshikawa, H. and Itoh, K. (2011). Changes in cell migration of mesenchymal cells during osteogenic differentiation. *FEBS Lett.* **585**, 4018–4024.
- Jagannathan, S., Horn, B. K. P., Ratilal, P. and Makris, N. C. (2011). Force estimation and prediction from time-varying density images. *IEEE Trans. Pattern Anal. Mach. Intell.* **33**, 1132–1146.
- Janmey, P. A. and McCulloch, C. A. (2007). Cell mechanics: integrating cell responses to mechanical stimuli. *Annu. Rev. Biomed. Eng.* **9**, 1–34.
- Key, Y.-S. and Robinson, D. N. (2013). Micropipette aspiration for studying cellular mechanosensory responses and mechanics. *Methods Mol. Biol.* **983**, 367–382.
- Kilarski, W. W., Güç, E., Teo, J. C. M., Oliver, S. R., Lund, A. W. and Swartz, M. A. (2013). Intravital immunofluorescence for visualizing the microcirculatory and immune microenvironments in the mouse ear dermis. *PLoS ONE* **8**, e57135.
- Kim, S. and Coulombe, P. A. (2010). Emerging role for the cytoskeleton as an organizer and regulator of translation. *Nat. Rev. Mol. Cell Biol.* **11**, 75–81.
- Kumar, S. (2014). Cellular mechanotransduction: stiffness does matter. *Nat. Mater.* **13**, 918–920.
- Lamprecht, M. R., Sabatini, D. M. and Carpenter, A. E. (2007). CellProfiler™: free, versatile software for automated biological image analysis. *Biotechniques* **42**, 71–75.
- Lemmon, C. A. and Romer, L. H. (2010). A predictive model of cell traction forces based on cell geometry. *Biophys. J.* **99**, L78–L80.
- Levental, K. R., Yu, H., Kass, L., Lakins, J. N., Egeblad, M., Erler, J. T., Fong, S. F. T., Csiszar, K., Giaccia, A., Weninger, W. et al. (2009). Matrix crosslinking forces tumor progression by enhancing integrin signaling. *Cell* **139**, 891–906.
- Li, K., Miller, E. D., Chen, M., Kanade, T., Weiss, L. E. and Campbell, P. G. (2008). Cell population tracking and lineage construction with spatiotemporal context. *Med. Image Anal.* **12**, 546–566.

- Lim, C. T., Zhou, E. H. and Quek, S. T. (2006). Mechanical models for living cells—a review. *J. Biomech.* **39**, 195-216.
- Lim, C. T., Bershadsky, A. and Sheetz, M. P. (2010). Mechanobiology. *J. R. Soc. Interface* **7** Suppl. 3, S291-S293.
- Massiera, G., Van Citters, K. M., Biancaniello, P. L. and Crocker, J. C. (2007). Mechanics of single cells: rheology, time dependence, and fluctuations. *Biophys. J.* **93**, 3703-3713.
- Medema, J. P. and Vermeulen, L. (2011). Microenvironmental regulation of stem cells in intestinal homeostasis and cancer. *Nature* **474**, 318-326.
- Miura, K. (2005). Tracking movement in cell biology. *Adv. Biochem. Eng. Biotechnol.* **95**, 267-295.
- Modersitzki, J. (2004). Numerical methods for image registration (ed. G. H. Golub, C. Schwab and E. Suli) Oxford University Press, Oxford, UK.
- Mrass, P., Takano, H., Ng, L. G., Daxini, S., Lasaro, M. O., Iparraguirre, A., Cavanagh, L. L., von Andrian, U. H., Ertl, H. C. J., Haydon, P. G. et al. (2006). Random migration precedes stable target cell interactions of tumor-infiltrating T cells. *J. Exp. Med.* **203**, 2749-2761.
- Mullins, R. D. (2010). Cytoskeletal mechanisms for breaking cellular symmetry. *Cold Spring Harb. Perspect. Biol.* **2**, a003392.
- Nourshargh, S., Hordijk, P. L. and Sixt, M. (2010). Breaching multiple barriers: leukocyte motility through venular walls and the interstitium. *Nat. Rev. Mol. Cell Biol.* **11**, 366-378.
- Overstreet, M. G., Gaylo, A., Angermann, B. R., Hughson, A., Hyun, Y.-M., Lambert, K., Acharya, M., Billroth-Maclurg, A. C., Rosenberg, A. F., Topham, D. J. et al. (2013). Inflammation-induced interstitial migration of effector CD4⁺ T cells is dependent on integrin α V. *Nat. Immunol.* **14**, 949-958.
- Pisano, M., Triacca, V., Barbee, K. A. and Swartz, M. A. (2015). An in vitro model of the tumor-lymphatic microenvironment with simultaneous transendothelial and luminal flows reveals mechanisms of flow enhanced invasion. *Integr. Biol.* **7**, 525-533.
- Polacheck, W. J., Charest, J. L. and Kamm, R. D. (2011). Interstitial flow influences direction of tumor cell migration through competing mechanisms. *Proc. Natl. Acad. Sci. USA* **108**, 11115-11120.
- Provenzano, P. P. and Keely, P. J. (2011). Mechanical signaling through the cytoskeleton regulates cell proliferation by coordinated focal adhesion and Rho GTPase signaling. *J. Cell Sci.* **124**, 1195-1205.
- Provenzano, P. P., Eliceiri, K. W., Campbell, J. M., Inman, D. R., White, J. G. and Keely, P. J. (2006). Collagen reorganization at the tumor-stromal interface facilitates local invasion. *BMC Med.* **4**, 38.
- Schneider, C. A., Rasband, W. S. and Eliceiri, K. W. (2012). ImageJ: 25 years of image analysis. *Nat. Methods* **9**, 671-675.
- Solon, J., Levental, I., Sengupta, K., Georges, P. C. and Janmey, P. A. (2007). Fibroblast adaptation and stiffness matching to soft elastic substrates. *Biophys. J.* **93**, 4453-4461.
- Suresh, S. (2007). Biomechanics and biophysics of cancer cells. *Acta Biomater.* **3**, 413-438.
- Swaminathan, V., Mythreye, K., Tim O'Brien, E., Berchuck, A., Blobel, G. C. and Superfine, R. (2011). Mechanical stiffness grades metastatic potential in patient tumor cells and in cancer cell lines. *Cancer Res.* **71**, 5075-5080.
- Titushkin, I. and Cho, M. (2007). Modulation of cellular mechanics during osteogenic differentiation of human mesenchymal stem cells. *Biophys. J.* **93**, 3693-3702.
- Vural, E. and Frossard, P. (2013). Analysis of descent-based image registration. *SIAM J. Imaging Sci.* **6**, 2310-2349.
- Wilson, E. H., Harris, T. H., Mrass, P., John, B., Tait, E. D., Wu, G. F., Pepper, M., Wherry, E. J., Dzierzinski, F., Roos, D. et al. (2009). Behavior of parasite-specific effector CD8⁺ T cells in the brain and visualization of a kinesis-associated system of reticular fibers. *Immunity* **30**, 300-311.
- Wirtz, D. (2009). Particle-tracking microrheology of living cells: principles and applications. *Annu. Rev. Biophys.* **38**, 301-326.
- Xie, J., Huppa, J. B., Newell, E. W., Huang, J., Ebert, P. J. R., Li, Q.-J. and Davis, M. M. (2012). Photocrosslinkable pMHC monomers stain T cells specifically and cause ligand-bound TCRs to be "preferentially" transported to the cSMAC. *Nat. Immunol.* **13**, 674-680.
- Yourek, G., Hussain, M. A. and Mao, J. J. (2007). Cytoskeletal changes of mesenchymal stem cells during differentiation. *ASAIO J.* **53**, 219-228.
- Zielinski, R., Mihai, C., Kniss, D. and Ghadiali, S. N. (2013). Finite element analysis of traction force microscopy: influence of cell mechanics, adhesion, and morphology. *J. Biomech. Eng.* **135**, 071009.
- Zitová, B. and Flusser, J. (2003). Image registration methods: a survey. *Image Vis. Comput.* **21**, 977-1000.